

# Theoretical Investigation of Two-Dimensional FeC<sub>4</sub> Structures with Surface Van Hove Singularity for Electrochemical Nitric Oxide Reduction Reaction

Yaowei Xiang, Meijie Wang, Yuxing Lin, Yaxin Zhao, Shunqing Wu, Yang Sun, Zi-Zhong Zhu, and Xinrui Cao\*



Cite This: *J. Phys. Chem. Lett.* 2025, 16, 475–482



Read Online

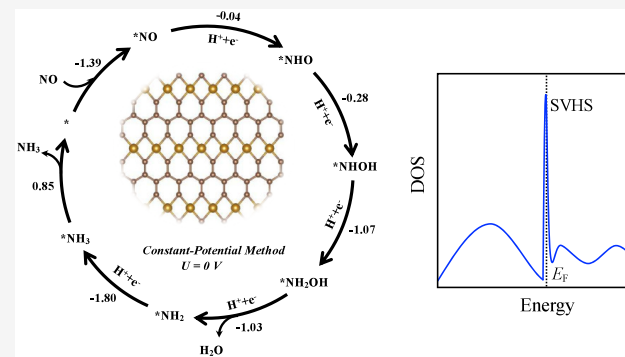
ACCESS |

Metrics & More

Article Recommendations

Supporting Information

**ABSTRACT:** The electrochemical nitric oxide reduction reaction (eNORR) is an efficient method for converting aqueous NO into NH<sub>3</sub>. The pursuit of innovative electrocatalysts with enhanced activity, selectivity, durability, and cost-effectiveness for NORR remains a research focus. In this study, using particle swarm optimization (PSO) searches, density functional theory (DFT), and the constant-potential method (CPM), we predict two stable two-dimensional FeC<sub>4</sub> monolayers, designated as  $\alpha$ -FeC<sub>4</sub> and  $\beta$ -FeC<sub>4</sub>, as promising electrocatalysts for the NORR. Our results demonstrate that both  $\alpha$ -FeC<sub>4</sub> and  $\beta$ -FeC<sub>4</sub> monolayers possess intrinsic metallicity with surface Van Hove singularity (SVHS), showing remarkable NORR catalytic performance. Additionally, the substantial disparity in adsorption free energies between NO and H atom at 0 V ensures the high selectivity of these novel FeC<sub>4</sub> monolayers toward NORR. These findings not only contribute to the expanding family of two-dimensional transition metal carbides but also provide a new idea for the design of highly efficient NORR electrocatalysts.



Nitric oxide (NO) is a major atmospheric pollutant, causing significant environmental damage. Currently, the mitigation of NO emissions has garnered considerable attention in environmental research and policy-making. Selective catalytic reduction (SCR) technology is employed by the prevailing industrial standard for NO removal, which uses ammonia (NH<sub>3</sub>) or hydrogen (H<sub>2</sub>) as reducing agents to convert NO into N<sub>2</sub> at temperatures exceeding 300 °C.<sup>1–3</sup> Presently, NH<sub>3</sub> production relies heavily on the Haber–Bosch process, which is characterized by high energy consumption and significant CO<sub>2</sub> emissions.<sup>4–6</sup> Therefore, the SCR approach raises significant concerns regarding its economic feasibility and environmental sustainability.<sup>7,8</sup> In light of these challenges, there is an urgent need to develop more sustainable and cost-effective NO removal strategies.

A recently proposed strategy known as the electrochemical nitric oxide reduction reaction (eNORR) has been proposed, which facilitates the dual process of eliminating NO while simultaneously producing NH<sub>3</sub>.<sup>9,10</sup> To date, various NORR catalysts have been reported, including pure metal-based catalysts such as Pt, Au, and Cu.<sup>10–13</sup> In addition, several two-dimensional materials have been explored for NORR, such as Si-N<sub>4</sub> embedded graphene,<sup>14</sup> MoN<sub>3</sub>/BP,<sup>15</sup> Cu<sub>2</sub>@GDY,<sup>16</sup> MnO<sub>4</sub>-hexaiminotriphenylene,<sup>17</sup> and Cu@g-C<sub>3</sub>N<sub>4</sub>.<sup>18</sup>

Two-dimensional transition metal carbides (TMCs) have attracted significant attention in both experimental and theoretical studies due to their high specific activity, excellent conductivity, and thermal stability,<sup>19,20</sup> showing high promise in the oxygen reduction reaction (ORR), hydrogen evolution reaction (HER), nitrogen reduction reaction (NRR), and carbon dioxide reduction reaction (CO<sub>2</sub>RR).<sup>21–24</sup> It is noted that numerous TMN<sub>4</sub> and TMB<sub>4</sub> monolayers, such as BeN<sub>4</sub>,<sup>25</sup> r-FeN<sub>4</sub>,<sup>26</sup> CrN<sub>4</sub>,<sup>27</sup> FeB<sub>4</sub>,<sup>28</sup> and TiB<sub>4</sub>,<sup>29</sup> have been theoretically and experimentally discovered. Given the periodic table positioning of carbon between boron and nitrogen, coupled with its comparable electronic properties, there is considerable potential for analogous carbon-based structures. Furthermore, the extensive use of Fe-based catalysts in ammonia synthesis reactions raises an intriguing question: is there a two-dimensional (2D) FeC<sub>4</sub>, and does it hold promise for application in NORR?

Received: November 21, 2024

Revised: December 22, 2024

Accepted: December 27, 2024

Published: January 2, 2025



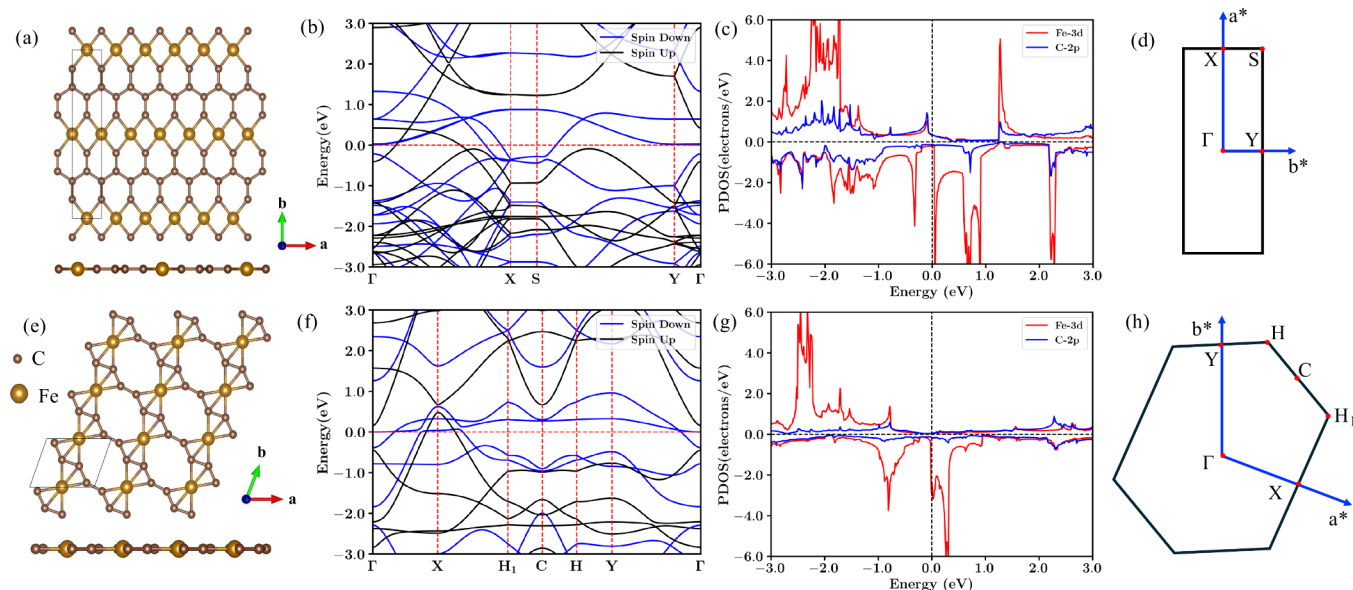


**Figure 1.** Top and side views of the two-dimensional FeC<sub>4</sub>: (a)  $\alpha$ -FeC<sub>4</sub> and (e)  $\beta$ -FeC<sub>4</sub>. The black lines represent the unit cell. Band structure and partial density of states (PDOS) of (b, c)  $\alpha$ -FeC<sub>4</sub> and (f, g)  $\beta$ -FeC<sub>4</sub>. Schematic diagram of the two-dimensional Brillouin zone in (d)  $\alpha$ -FeC<sub>4</sub> and (h)  $\beta$ -FeC<sub>4</sub>. High symmetry point coordinates:  $\Gamma$  (0, 0, 0), X (0.5, 0, 0), H<sub>1</sub> (0.71, 0.42, 0), C (0.5, 0.5, 0), H (0.29, 0.58, 0), Y (0, 0.5, 0), and S (0.5, 0.5, 0).

To address these inquiries, we conducted a structural search of 2D FeC<sub>4</sub> and predicted two novel FeC<sub>4</sub> monolayers with superior thermodynamical, dynamical, and mechanical stability. Their potential applications in the NORR were explored, and the corresponding catalytic mechanism was elucidated using density functional theory (DFT) and the constant-potential method (CPM). Our findings reveal that these two structures demonstrate remarkably high catalytic activity and selectivity for NORR. We anticipate that our research will not only enrich the growing family of 2D transition metal carbides but also offer novel insights for the development of highly efficient NORR electrocatalysts.

A stoichiometric ratio of Fe:C = 1:4 was chosen for a comprehensive particle swarm optimization (PSO) search. Following an extensive exploration of possible structures, two low-energy structures were discovered, designated as  $\alpha$ -FeC<sub>4</sub> and  $\beta$ -FeC<sub>4</sub>. The unit cell of  $\alpha$ -FeC<sub>4</sub> contains two Fe atoms and eight C atoms, as illustrated in Figure 1a. It belongs to the *Cmmm* space group, with optimized lattice constants of  $a = 2.44 \text{ \AA}$  and  $b = 12.79 \text{ \AA}$ . The Fe atom adopts a hexacoordinated coordinate configuration, bonding with four C atoms and two adjacent Fe atoms. The Fe atoms form linear chains with an intrachain distance of 2.44 Å and an interchain distance of 6.51 Å. For  $\beta$ -FeC<sub>4</sub> (Figure 1e), its unit cell comprises one Fe atom and four C atoms, adopting the *P2/m* space group, with the optimized lattice dimensions of  $a = 5.09 \text{ \AA}$  and  $b = 3.73 \text{ \AA}$ . Distinct from the  $\alpha$ -FeC<sub>4</sub> monolayer, the Fe atom in the  $\beta$ -FeC<sub>4</sub> monolayer is hexa-coordinated, engaging in bonds with six carbon atoms to form a planar geometry, with Fe-C bond distances ranging from 1.96 to 2.03 Å. Additionally, the nearest neighbor, second nearest neighbor, and third nearest neighbor distances among Fe atoms are 3.73, 5.09, and 7.32 Å, respectively. In  $\alpha$ -FeC<sub>4</sub> and  $\beta$ -FeC<sub>4</sub>, the magnetic moments of each Fe atom are 1.64  $\mu_B$  and 1.86  $\mu_B$ , respectively. This is consistent with the results obtained from the spin density (Figure S1e,f), which shows that the spin density is mainly concentrated on the Fe atoms.

To better understand the bonding features of 2D FeC<sub>4</sub>, we calculated the electron localization function (ELF)<sup>30</sup> as illustrated in Figure S1a,b. The ELF value ranges from 0 to 1, where values closer to 1 indicate a higher density of covalent electrons or lone pairs, whereas those closer to 0 suggest a lower charge density. Figure S1a,b illustrates that the predicted two 2D FeC<sub>4</sub> exhibit ionic bonding between Fe and C atoms, while the bonds between carbon atoms are bonded covalently. The different colored areas in the ELF maps highlight the electron transfer from Fe atoms to C atoms. Bader charge analysis further reveals that the Fe atom in  $\alpha$ -FeC<sub>4</sub> donates 0.78  $e^-$  to C atoms, while the Fe atom in  $\beta$ -FeC<sub>4</sub> transfers 0.90  $e^-$  to C atoms. Additionally, we calculated the charge density difference maps, as shown in Figure S1c,d, which align with the ELF results.

Typically, metallic characteristics are an essential requirement for a superior electrocatalyst. Therefore, we calculated the density of states (PDOS) diagrams and band structures of  $\alpha$ -FeC<sub>4</sub> and  $\beta$ -FeC<sub>4</sub>. The Brillouin zones of  $\alpha$ -FeC<sub>4</sub> and  $\beta$ -FeC<sub>4</sub> and their high symmetry points are shown in Figure 1d,h. The calculation results (Figure 1b,f) show that the energy bands of  $\alpha$ -FeC<sub>4</sub> and  $\beta$ -FeC<sub>4</sub> both cross the Fermi level ( $E_F$ ), suggesting their metallic nature, which is beneficial for efficient charge transfer during electrocatalytic processes. The PDOS diagrams (Figure 1c,g) reveal that near the Fermi level ( $E_F$ ), the spin-up channels are primarily contributed by Fe 3d and C 2p orbitals, while the spin-down channels are predominantly derived from Fe 3d orbitals. Both  $\alpha$ -FeC<sub>4</sub> and  $\beta$ -FeC<sub>4</sub> exhibit large density of states at the  $E_F$ , aligning well with  $E_F$ , which is characteristic of surface Van Hove singularity (SVHS). Such SVHS is associated with flat energy bands along Y- $\Gamma$ -X in  $\alpha$ -FeC<sub>4</sub> and  $\Gamma$ -X-H<sub>1</sub> in  $\beta$ -FeC<sub>4</sub>, which facilitate electron transfer and enhance chemical reactivity toward adsorbates. Studies have shown that SVHS can serve as an electron bath, enhancing the adsorption of O<sub>2</sub> and subsequent reactions.<sup>31</sup> It is hypothesized that  $\alpha$ -FeC<sub>4</sub> and  $\beta$ -FeC<sub>4</sub> with SVHS may also exhibit excellent catalytic effects in electrocatalysis. Moreover, there is

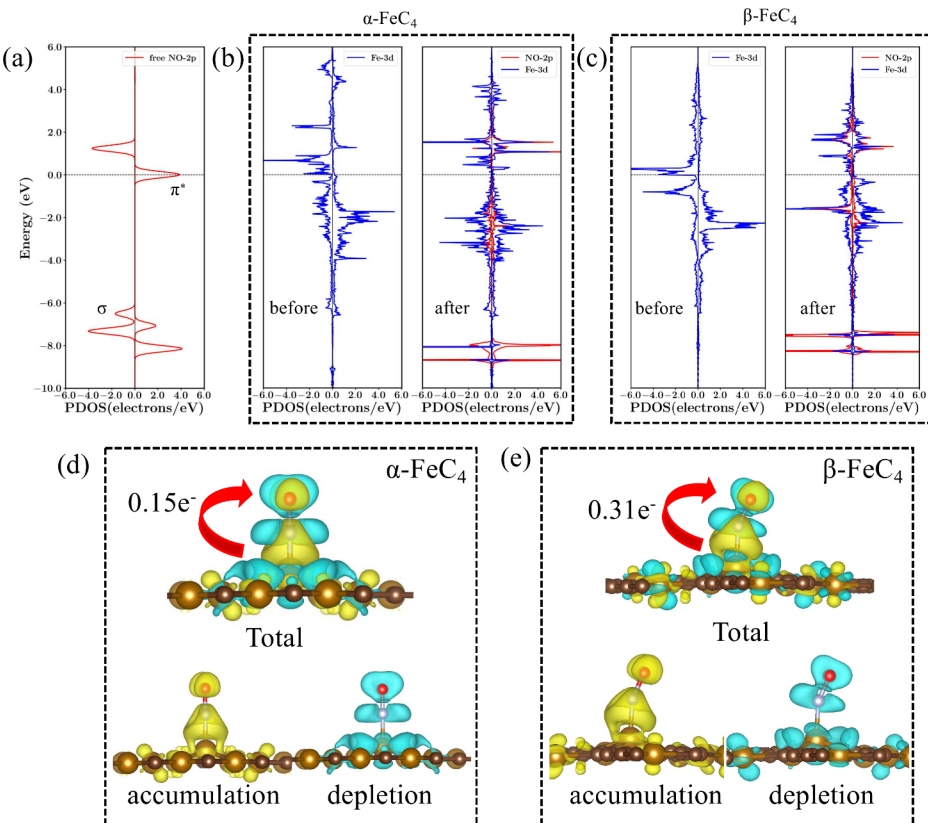


**Figure 2.** (a) PDOS diagram of NO molecules. PDOS of NO 2p and Fe 3d orbitals before and after NO adsorption on (b)  $\alpha\text{-FeC}_4$  and (c)  $\beta\text{-FeC}_4$ . Charge density difference of the NO adsorption on (d)  $\alpha\text{-FeC}_4$  and (e)  $\beta\text{-FeC}_4$ . The isosurface value is  $0.002 \text{ e}/\text{\AA}^3$ , and charge accumulation and depletion are colored yellow and cyan, respectively.

significant hybridization between the Fe 3d orbitals and C 2p orbitals near the  $E_F$ , indicating strong interaction between Fe and C atoms. Such strong interactions are crucial for enhancing the stability of these materials.

To verify the stability of the two predicted low-energy structures, we evaluated their mechanical, dynamical, and thermodynamical stabilities.

First, we calculated their cohesive energies ( $E_{\text{coh}}$ ), using the following equation:

$$E_{\text{coh}} = \frac{nE_{\text{Fe}} + mE_{\text{C}} - E_{\text{tot}}}{m + n} \quad (1)$$

where  $E_{\text{Fe}}$  and  $E_{\text{C}}$  represent the total energies of isolated Fe and C atoms, respectively, and  $E_{\text{tot}}$  is the total energy of the 2D FeC<sub>4</sub>. Here,  $m$  and  $n$  denote the number of C and Fe atoms in the simulated unit cell of 2D FeC<sub>4</sub>, respectively. The calculated cohesive energies for  $\alpha\text{-FeC}_4$  and  $\beta\text{-FeC}_4$  are 6.70 and 6.44 eV/atom, respectively, which are higher than those of  $t\text{-FeC}$  (5.76 eV/atom),<sup>32</sup> FeB<sub>2</sub> (4.87 eV/atom),<sup>33</sup>  $\alpha\text{-FeB}_6$  (5.79 eV/atom),<sup>34</sup> and BeN<sub>4</sub> (4.83 eV/atom),<sup>35</sup> showing comparable stability of these reported 2D materials.

Next, we assessed the mechanical stabilities of  $\alpha\text{-FeC}_4$  and  $\beta\text{-FeC}_4$  under lattice distortions by calculating their elastic constants. For mechanically stable two-dimensional materials, their elastic constants must satisfy the Born–Huang criteria:<sup>36</sup>

$C_{11}C_{22} - C_{12}^2 > 0$  and  $C_{66} > 0$ . As shown in Table S1, both  $\alpha\text{-FeC}_4$  and  $\beta\text{-FeC}_4$  meet these requirements, confirming their mechanical stability.

Then, the dynamical and thermodynamical stabilities of the two FeC<sub>4</sub> monolayers are evaluated by phonon dispersion

spectral calculation and AIMD simulations at varying temperatures. As shown in Figure S2a,e, the absence of imaginary phonon modes throughout the Brillouin zone confirms that both  $\alpha\text{-FeC}_4$  and  $\beta\text{-FeC}_4$  are dynamically stable. Furthermore, geometry snapshots captured at 10 ps reveal that both  $\alpha\text{-FeC}_4$  and  $\beta\text{-FeC}_4$  retain their initial structures at temperatures of 300, 600, and 900 K, thereby confirming their thermal stability under these conditions (Figure S2b–d,f–h).

Overall, both  $\alpha\text{-FeC}_4$  and  $\beta\text{-FeC}_4$  possess good mechanical, thermodynamical, and dynamical stabilities.

The efficient adsorption of NO is a critical prerequisite for the progression of the NORR, and thereby, we conducted a comprehensive evaluation of all potential adsorption configurations, as illustrated in Figure S3a. Given the 2.44 Å interatomic distance between adjacent Fe atoms in the  $\alpha\text{-FeC}_4$  monolayer, cooperative adsorption of NO by two Fe atoms is plausible. For the  $\alpha\text{-FeC}_4$  system, six configurations are considered according to the possible adsorption pattern and active sites, which are N-end, O-end, NO-side, O-bridge, N-bridge, and NO-bridge. After structural optimizations, we identified three representative chemical adsorption configurations and one physical adsorption configuration, as depicted in Figure S3b. The adsorption energies for the N-end, N-bridge, NO-bridge, and O-end configurations are -2.00, -1.52, -1.51, and -0.33 eV, respectively. The other two configurations, namely, the NO-side and O-bridge, transition into N-end and O-end configurations, respectively. For the  $\beta\text{-FeC}_4$  monolayer, the larger interatomic distance of adjacent Fe atoms (3.73 Å) precludes the possibility of bridge adsorption, so only the N-end, O-end, and NO-side configurations are

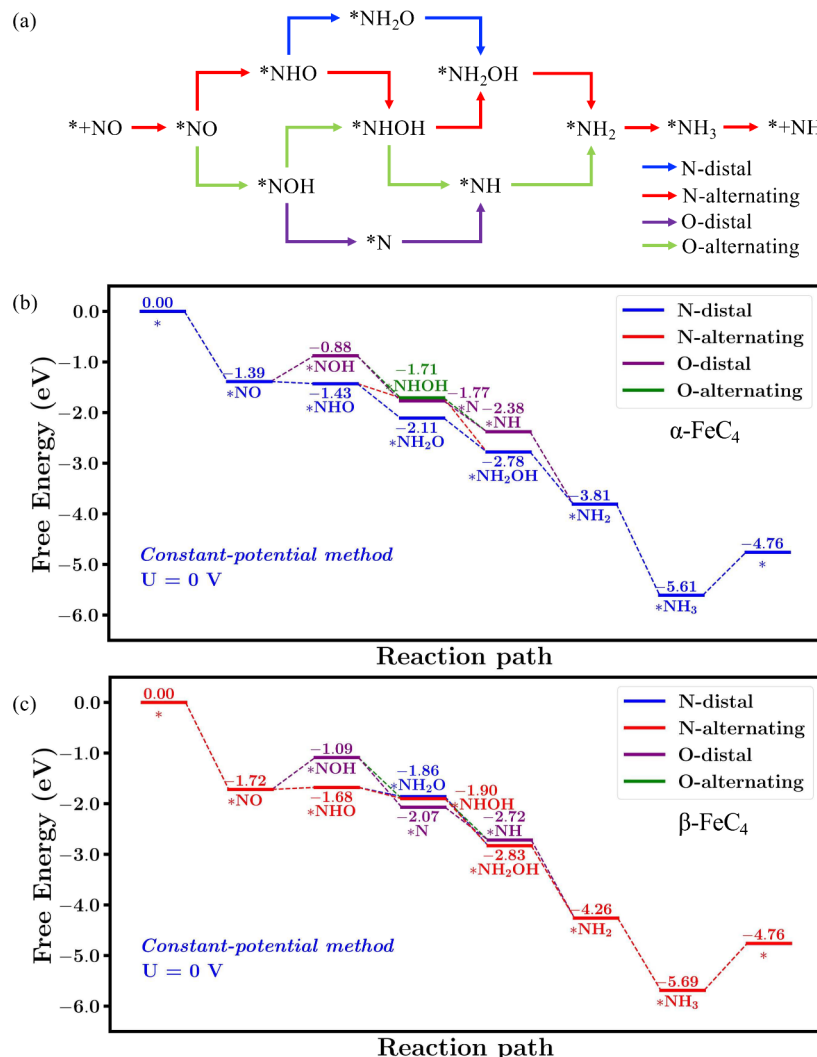


**Figure 3.** (a) Schematic illustration of the four main reaction pathways for the electrochemical reduction of NO to NH<sub>3</sub>. The free energy diagram of the NORR for (b)  $\alpha\text{-FeC}_4$  and (c)  $\beta\text{-FeC}_4$  at an applied potential of 0 V under the implicit solvation model.

considered. Notably, the NO-side configuration spontaneously converts to the N-end after geometry optimizations. For the other two adsorption patterns, the adsorption energies for the N-end and O-end configurations are -2.10 and -0.67 eV, respectively, as shown in Figure S3c.

Both  $\alpha\text{-FeC}_4$  and  $\beta\text{-FeC}_4$  exhibit strong adsorption for NO and have the presence of SVHS. Therefore, taking the structural motif of  $\alpha\text{-FeC}_4$  as an example, we explored the electronic properties and the corresponding NO adsorption abilities for a series of  $\alpha\text{-MC}_4$  (M = Mn, Co, Ni, and Cu). As shown in Figure S4, the position of the SVHS can be tuned by the substituted transition metals. Among them, the position of the SVHS of  $\alpha\text{-MnC}_4$  is the closest to the Fermi level with a higher peak intensity compared to  $\alpha\text{-FeC}_4$ , while the SVHS in  $\alpha\text{-CuC}_4$  is far from the Fermi level.

Then, we investigated the adsorption of NO on these different  $\alpha\text{-MC}_4$  materials, and the adsorption energies are -2.87, -2.0, -1.20, -0.75, and -0.42 eV for  $\alpha\text{-MnC}_4$ ,  $\alpha\text{-FeC}_4$ ,  $\alpha\text{-CoC}_4$ ,  $\alpha\text{-NiC}_4$ , and  $\alpha\text{-CuC}_4$ , respectively. Obviously, the one with SVHS exhibits a higher NO adsorption ability. To better understand the role of SVHS in NO capture, we explored the relation between the density of states at the Fermi level and the NO adsorption energy. For simplicity, the value of the density

of states at the Fermi level is labeled as SVHS, even though SVHS does not exist in  $\alpha\text{-CuC}_4$ . As depicted in Figure S5a, the greater the intensity of the SVHS, the stronger the adsorption interaction of NO. Additionally, a linear relationship is observed between SVHS peak intensity and NO adsorption energy (Figure S5b), with a fitting coefficient of  $R^2 = 0.982$ , indicating a strong positive correlation between the SVHS and NO adsorption energy. These results suggest that the intensity and position of SVHS may affect the adsorption behavior of NO by regulating the electronic density of states distribution. Specifically, when the SVHS is closer to the Fermi level, the NO adsorption capacity appears to be stronger.

In view of the disappearance of SVHS in  $\alpha\text{-CuC}_4$ , we further constructed the  $\alpha\text{-CuFeC}_8$  monolayer by partially replacing Fe atoms (Figure S6a,d). It can be seen in the obtained PDOS (Figure S6b,e) of  $\alpha\text{-CuFeC}_8$  that SVHS persists, which is predominantly contributed by Fe atoms. In addition, analysis of NO adsorption on Fe and Cu atoms within the  $\alpha\text{-CuFeC}_8$  structure (Figure S6c,f) indicates that NO molecules preferentially adsorb on Fe atoms, and the one with stronger SVHS intensity shows better NO adsorption ability. This finding underscores that the localized nature of SVHS can

modulate the adsorption behavior and corresponding catalytic activity.

To gain deeper insights into the interaction between NO molecules and 2D FeC<sub>4</sub>, we calculated the PDOS and charge density difference diagrams for the most stable N-end adsorption configuration on 2D FeC<sub>4</sub>. As depicted in Figure 2a–c, significant hybridization occurs between the NO 2p and Fe 3d orbitals, indicating a strong interaction between NO and the substrate. Bader charge analysis reveals that the adsorbed NO molecules gain 0.15 and 0.31 e from  $\alpha$ -FeC<sub>4</sub> and  $\beta$ -FeC<sub>4</sub>, respectively. The charge density difference diagrams (Figure 2d,e) further illustrate the redistribution of electrons upon adsorption, with electron accumulation and depletion observed on both the adsorbed NO and the substrate. To better understand the interaction between the five 3d orbitals of the Fe atom and NO, we performed a detailed analysis of the d orbital energy level distribution of Fe atoms of  $\alpha$ -FeC<sub>4</sub> and  $\beta$ -FeC<sub>4</sub> before and after adsorption of NO molecules. As shown in Figure S7a, before NO adsorption, the d<sub>z<sup>2</sup></sub>, d<sub>xz</sub>, and d<sub>yz</sub> orbitals of the Fe atom in  $\alpha$ -FeC<sub>4</sub> have a higher density of states distribution near the Fermi level. This suggests that these orbitals are highly chemically active and may play a key role in interactions with adsorbed molecules. After NO adsorption (Figure S7b), the density of states distribution for the d<sub>z<sup>2</sup></sub>, d<sub>xz</sub>, and d<sub>yz</sub> orbitals of Fe undergoes a notable change near the Fermi level, indicating that the electrons in these orbitals participate in bonding interactions with NO through orbital mixing hybridization. In particular, the d<sub>z<sup>2</sup></sub> orbital interacts with the NO  $\sigma$  orbital during the adsorption process (Figure S7c), forming occupied and unoccupied  $\sigma$ -d<sub>z<sup>2</sup></sub> orbitals, and the d<sub>xz</sub> and d<sub>yz</sub> orbitals of Fe interact with the  $\pi$  and  $\pi^*$  orbitals of NO. By calculating the changes of the number of electrons in the Fe d orbitals before and after NO adsorption (Table S2), it can be found that the number of electrons in the d<sub>z<sup>2</sup></sub> and d<sub>xz</sub> orbitals increases, while the number of electrons in the d<sub>yz</sub> orbital decreases. This indicates that the d<sub>xz</sub> orbitals interact with the  $\pi$ -type 2p orbitals of NO, whereas the d<sub>yz</sub> orbitals interact with the  $\pi^*$ -type 2p orbitals of NO. The interactions among the d orbitals of Fe and the  $\sigma$ ,  $\pi$ , and  $\pi^*$  orbitals of NO are responsible for the NO adsorption. Through the redistribution of electronic states, electrons from the occupied 3d orbitals of Fe atoms are transferred to the partially occupied  $\pi^*$  orbitals of NO, while electrons in the NO  $\sigma$  orbitals are donated back to the Fe 3d orbitals, resulting in the net electron transfer to NO. This electron donation/back-donation mechanism significantly weakens the NO bond (from 1.169 to 1.174 Å). A similar activation mechanism is also observed on  $\beta$ -FeC<sub>4</sub> (Figure S8), and the NO bond length increases from 1.169 to 1.187 Å.

Starting from the most stable NO adsorption configuration, we investigated four main reaction pathways for the conversion of NO to NH<sub>3</sub> (Figure 3a): N-distal, O-distal, N-alternating, and O-alternating.

The structural optimizations of potential intermediates during the NORR process for the four pathways were conducted using VASP, with the most stable configurations depicted in Figures S9 and S10. Then, the influence of external potentials and solvation effects was evaluated by using JDFTx. The NORR free energy diagrams for all considered pathways, calculated using the constant-potential method at 0 V, are presented in Figure 3b,c.

For  $\alpha$ -FeC<sub>4</sub>, the Gibbs free energy decreases by 1.39 eV when a NO molecule is adsorbed in the N-end pattern. For the first hydrogenation step, the hydrogen proton pair may attack

either the N site or the O site of activated \*NO, resulting in the formation of \*NHO or \*NOH, respectively. The former process is exothermic, with a free energy decrease of 0.04 eV, whereas the latter one is endothermic and involves an increase in free energy of 0.51 eV, suggesting that \*NHO generation is more energy favored. When \*NHO is generated, it can be further hydrogenated to form \*NHOH or \*NH<sub>2</sub>O, which correspond to the N-alternating pathway and the N-distal pathway, respectively. As depicted in Figure 3b, the free energy changes for the formation of \*NHOH and \*NH<sub>2</sub>O are exothermic, with values of 0.28 and 0.68 eV, respectively. From an energy point of view, the generation of \*NHOH and \*NH<sub>2</sub>O is plausible. Further kinetic barrier calculations for the two hydrogenation processes, as discussed later, reveal that the N-alternating pathway is more likely to occur due to its significantly lower energy barrier. The subsequent hydrogenation of \*NHOH yields \*NH<sub>2</sub>OH, releasing an energy of 1.07 eV. In the fourth and fifth hydrogenation processes, \*NH<sub>2</sub>OH is initially protonated to form \*NH<sub>2</sub> + H<sub>2</sub>O, followed by the formation of NH<sub>3</sub>. These two steps are exothermic, with energy decreases of 1.03 and 1.80 eV, respectively. Finally, the desorption of the generated product NH<sub>3</sub> requires an energy of 0.85 eV. Similarly, we also calculated the free energy diagrams for the O-distal and O-alternating pathways. Apart from the hydrogenation of \*NO to \*NOH, which is endothermic with a free energy increase of 0.51 eV, the other hydrogenation steps are exothermic.

For  $\beta$ -FeC<sub>4</sub>, the four possible NORR reaction pathways were also evaluated, and the corresponding NORR free energy diagrams and optimized intermediates are shown in Figure 3c and Figure S10. In the first hydrogenation process, the free energy increases by 0.04 and 0.63 eV for the formation of \*NHO and \*NOH, respectively. Given the considerable energy demands for \*NOH formation, both the O-distal and O-alternating pathways in the NORR on  $\beta$ -FeC<sub>4</sub> are energetically unfavorable. When \*NHO forms on  $\beta$ -FeC<sub>4</sub>, all of the subsequent hydrogenation steps are exothermic. Therefore, the potential-determining step (PDS) for the NORR on  $\beta$ -FeC<sub>4</sub> is the first hydrogenation step (\*NO + H<sup>+</sup> + e<sup>-</sup> → \*NHO), and the limiting potential is -0.04 V, which is very low.

The overpotentials of  $\alpha$ -FeC<sub>4</sub> (0 V) and  $\beta$ -FeC<sub>4</sub> (-0.04 V) are comparable to or even lower than those of electrocatalysts evaluated using the constant-potential method, such as Co<sub>4</sub>N<sub>8</sub>-gra (-0.2 V),<sup>37</sup> MnO<sub>4</sub>-HTP (-0.19 V),<sup>17</sup> and Mn-COF@N (-0.005 V).<sup>38</sup> This indicates that both  $\alpha$ -FeC<sub>4</sub> and  $\beta$ -FeC<sub>4</sub> hold significant promise as high-performance candidates for NORR catalysis.

During the NORR process, N–N coupling is also possible. Consequently, we further explored the coupling between gaseous NO and N-end adsorbed NO. From Figure S11, one can see that such a coupling process on both  $\alpha$ -FeC<sub>4</sub> and  $\beta$ -FeC<sub>4</sub> is endothermic, with energy increases of 1.04 and 0.72 eV, respectively. It is worth noting that the two predicted novel 2D FeC<sub>4</sub> have multiple Fe sites, which enable the potential adsorption of one NO molecule per Fe atom. The energy of two adjacent Fe atoms each adsorbing one NO is 2.37 and 2.52 eV lower than that of the \*NO dimer adsorbed on a single Fe atom on  $\alpha$ -FeC<sub>4</sub> and  $\beta$ -FeC<sub>4</sub>, respectively. Clearly, NO molecules tend to be adsorbed individually on isolated Fe atoms even under a relatively higher NO concentration. Experimentally, the formation of \*NO dimers can be avoided

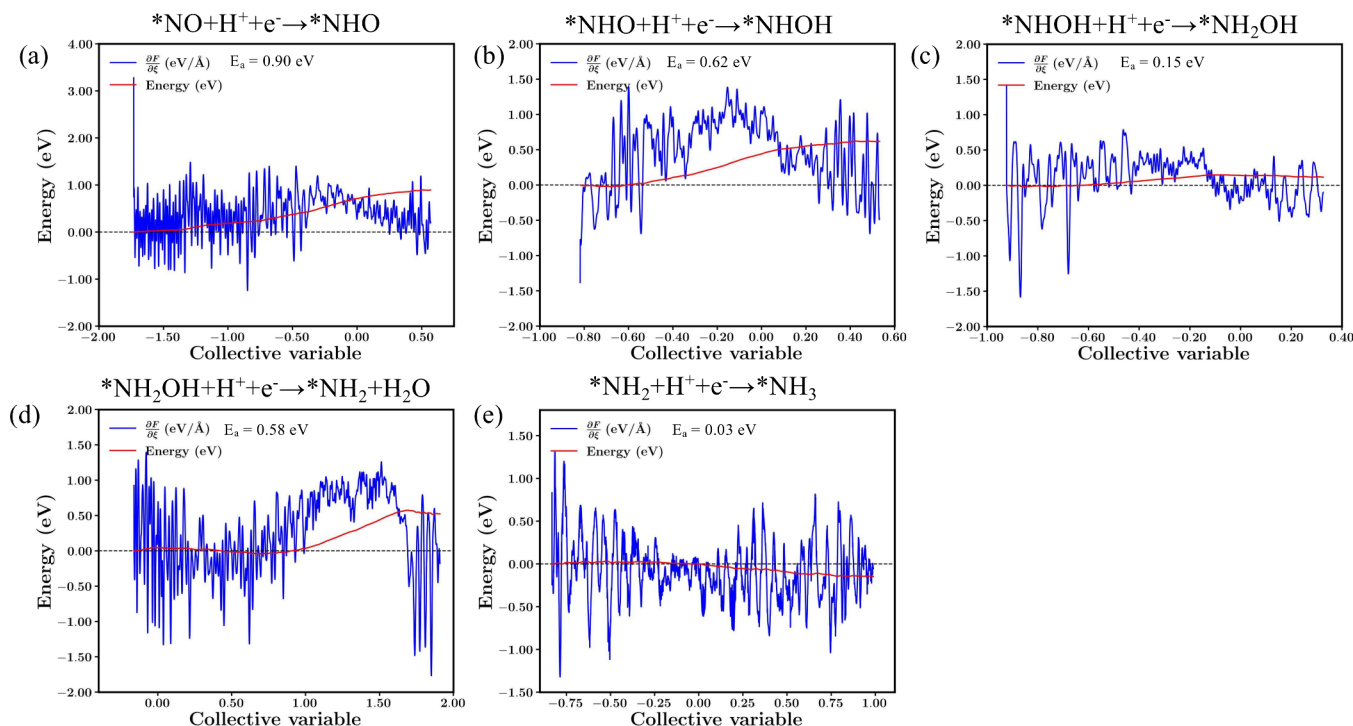


**Figure 4.** Calculated kinetic energy barriers for the N-alternating path of  $\alpha\text{-FeC}_4$ .

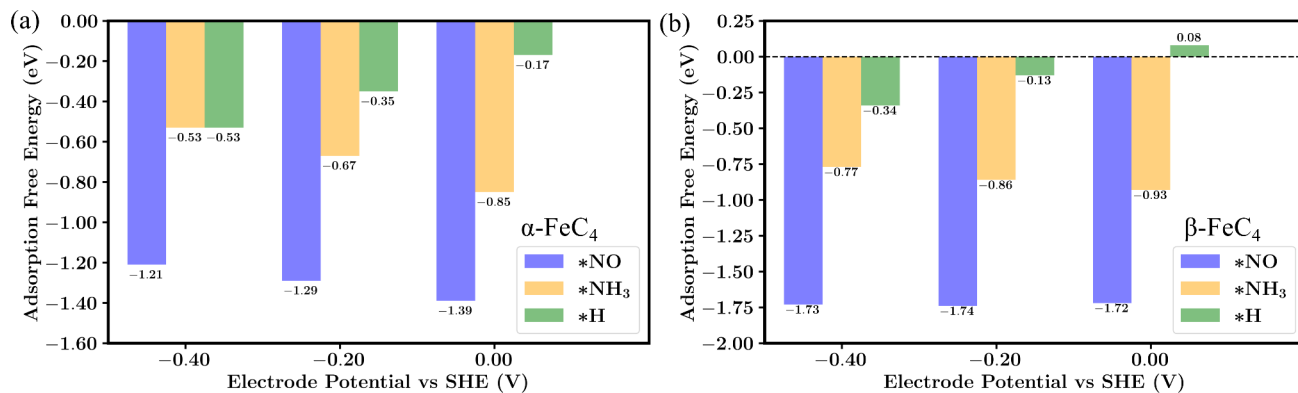


**Figure 5.** Calculated adsorption free energy of H, NO molecules, and  $\text{NH}_3$  molecules on (a)  $\alpha\text{-FeC}_4$  and (b)  $\beta\text{-FeC}_4$ .

by controlling the NO concentration.<sup>39</sup> Therefore, the selective generation of  $\text{NH}_3$  can be achieved on 2D  $\text{FeC}_4$ .

It is well-known that kinetic energy barriers are critical in catalytic reactions. Given that  $\alpha\text{-FeC}_4$  is thermodynamically superior to  $\beta\text{-FeC}_4$  in NORR, we primarily focus on the kinetic energy barriers during the hydrogenation step of the NORR on  $\alpha\text{-FeC}_4$ . To simulate a relatively real electrocatalytic environment, we introduced 62  $\text{H}_2\text{O}$  molecules and investigated the hydrogenation process using AIMD with a slow-growth method.

Since both the N-alternating and N-distal pathways are exothermic, it is imperative to assess the kinetic energy barriers associated with these two routes (Figure 4 and Figure S13a). The intermediate structures are shown in Figures S12 and S13b. The first hydrogenation of  $*\text{NO}$  to form  $*\text{NHO}$  involves an energy barrier of 0.90 eV (Figure 4a). Subsequently, the second hydrogenation of  $*\text{NOH}$  can yield either  $*\text{NH}_2\text{O}$  or  $*\text{NHOH}$ , which represents the only difference between the N-alternating and N-distal mechanisms. In the N-distal pathway, the energy barrier for  $*\text{NH}_2\text{O}$  formation is as high as 1.59 eV

(Figure S13a), while the H atom attacks the O atom in  $*\text{NHO}$  to generate  $*\text{NHOH}$  for the N-alternating pathway, which only requires a much lower energy barrier of 0.62 eV (Figure 4b). Therefore, the N-alternating pathway is kinetically more favorable. The kinetic energy barriers of the N-distal pathway hydrogenation process are no longer evaluated. When  $*\text{NHOH}$  is formed, further hydrogenation to form  $*\text{NH}_2\text{OH}$  only needs to overcome a low energy barrier of 0.15 eV (Figure 4c). In the fourth hydrogenation step, as the H atom from the water layer approaches  $*\text{NH}_2\text{OH}$ , the bond between  $*\text{NH}_2$  and OH weakens, facilitating the formation of  $\text{H}_2\text{O}$ . Then, the newly produced water molecule returns to the water layer. The energy barrier for this process is 0.58 eV (Figure 4d). Subsequently, the remaining  $*\text{NH}_2$  is then further hydrogenated to  $*\text{NH}_3$ , with a rather low energy barrier of 0.03 eV (Figure 4e). Based on these results, it is clear that the N-alternating pathway is the optimal NORR route, and its rate-determining step (RDS) in the kinetics is the first hydrogenation process.

Generally, the hydrogen evolution reaction (HER) is the primary competing reaction during the NORR process. Within our examined framework, both 2D FeC<sub>4</sub> monolayers show low H atom adsorption ability. Specifically, at an applied potential of 0 V (Figure 5), the adsorption free energy of the H atom on  $\alpha$ -FeC<sub>4</sub> and  $\beta$ -FeC<sub>4</sub> is -0.17 and 0.08 eV, respectively; for the adsorption of NO, the corresponding adsorption free energies on  $\alpha$ -FeC<sub>4</sub> and  $\beta$ -FeC<sub>4</sub> are -1.39 and -1.72 eV, respectively. The large energy difference effectively inhibits the competitive reaction, thereby ensuring a high NO selective adsorption.

It is known that the applied potential may affect the adsorption behavior, and evaluating the adsorption of H, NO, and NH<sub>3</sub> at different potentials is essential. In this study, the considered range for applied potential is from -0.2 to -0.4 V. As the potential becomes more negative, the adsorption strength of H increases on both  $\alpha$ -FeC<sub>4</sub> and  $\beta$ -FeC<sub>4</sub>, changing from -0.17 to -0.53 eV for  $\alpha$ -FeC<sub>4</sub> and from 0.08 to -0.34 eV for  $\beta$ -FeC<sub>4</sub>. For NH<sub>3</sub> adsorption, a different trend is observed, with values shifting from -0.85 to -0.53 eV on  $\alpha$ -FeC<sub>4</sub> and from -0.93 to -0.77 eV for  $\beta$ -FeC<sub>4</sub>. NO adsorption exhibits a subtle decrease in  $\alpha$ -FeC<sub>4</sub>, dropping from -1.39 to -1.21 eV, while in  $\beta$ -FeC<sub>4</sub>, the NO adsorption remains largely unchanged. Upon comparing the adsorption free energies, we demonstrate that the two predicted 2D FeC<sub>4</sub> exhibit a high selectivity for NORR within the examined potential range.

In summary, we successfully identified two 2D FeC<sub>4</sub> monolayer structures,  $\alpha$ -FeC<sub>4</sub> and  $\beta$ -FeC<sub>4</sub>, through an extensive structure search. First-principles calculations confirm their thermodynamical, dynamical, and mechanical stability. Both  $\alpha$ -FeC<sub>4</sub> and  $\beta$ -FeC<sub>4</sub> possess intrinsic metallicity along with surface Van Hove singularity (SVHS). The catalytic mechanism of the electrochemical reduction of NO to NH<sub>3</sub> on these monolayers was systematically investigated, and the optimal NORR routes were identified. The reported limiting potentials for these new 2D FeC<sub>4</sub> electrocatalysts are quite low. Moreover, both  $\alpha$ -FeC<sub>4</sub> and  $\beta$ -FeC<sub>4</sub> exhibit much stronger adsorption of NO compared to H and NH<sub>3</sub>, ensuring the high selectivity for NORR within the examined potential range. Our results demonstrate that both  $\alpha$ -FeC<sub>4</sub> and  $\beta$ -FeC<sub>4</sub> are promising NORR electrocatalysts with high catalytic activity and selectivity.

## ASSOCIATED CONTENT

### Supporting Information

The Supporting Information is available free of charge at <https://pubs.acs.org/doi/10.1021/acs.jpcllett.4c03349>.

Computational details, elastic constants  $C_{ij}$ , ELF maps, charge density difference diagrams, phonon spectra and AIMD simulations, adsorption configuration of NO, and free energy diagrams in related systems ([PDF](#))

## AUTHOR INFORMATION

### Corresponding Author

Xinrui Cao — Department of Physics and Fujian Provincial Key Laboratory of Theoretical and Computational Chemistry, Xiamen University, Xiamen 361005, China;  
[orcid.org/0000-0002-2998-8863](#); Email: [xinruicao@xmu.edu.cn](mailto:xinruicao@xmu.edu.cn)

### Authors

Yaowei Xiang — Department of Physics, Xiamen University, Xiamen 361005, China

Meijie Wang — Department of Physics, Xiamen University, Xiamen 361005, China; [orcid.org/0009-0008-2000-5438](#)

Yuxing Lin — Department of Physics, Xiamen University, Xiamen 361005, China

Yixin Zhao — Department of Physics, Xiamen University, Xiamen 361005, China

Shunqing Wu — Department of Physics, Xiamen University, Xiamen 361005, China; [orcid.org/0000-0002-2545-0054](#)

Yang Sun — Department of Physics, Xiamen University, Xiamen 361005, China; [orcid.org/0000-0002-4344-2920](#)

Zi-Zhong Zhu — Department of Physics, Xiamen University, Xiamen 361005, China; [orcid.org/0000-0001-5353-4418](#)

Complete contact information is available at:

<https://pubs.acs.org/10.1021/acs.jpcllett.4c03349>

### Notes

The authors declare no competing financial interest.

## ACKNOWLEDGMENTS

This work is supported by the National Natural Science Foundation of China (22073076 and 21933009) and the Fundamental Research Funds for the Central Universities of China (20720210023 and 20720240138). Xiamen University High Performance Computing Center is acknowledged for the supercomputer resources. Shaorong Fang and Tianfu Wu from the Information and Network Center of Xiamen University are acknowledged for the help with the GPU computing.

## REFERENCES

- (1) Koebel, M.; Madia, G.; Elsener, M. Selective Catalytic Reduction of NO and NO<sub>2</sub> at Low Temperatures. *Catal. Today* **2002**, *73*, 239–247.
- (2) Andana, T.; Rappé, K. G.; Gao, F.; Szanyi, J.; Pereira-Hernandez, X.; Wang, Y. Recent Advances in Hybrid Metal Oxide–Zeolite Catalysts for Low-Temperature Selective Catalytic Reduction of NO<sub>x</sub> by Ammonia. *Appl. Catal., B* **2021**, *291*, 120054.
- (3) Guan, Y.; Liu, Y.; Lv, Q.; Wang, B.; Che, D. Review on the Selective Catalytic Reduction of NO with H<sub>2</sub> by Using Novel Catalysts. *J. Environ. Chem. Eng.* **2021**, *9*, 106770.
- (4) Chen, J. G.; Crooks, R. M.; Seefeldt, L. C.; Bren, K. L.; Bullock, R. M.; Daresbourg, M. Y.; Holland, P. L.; Hoffman, B.; Janik, M. J.; Jones, A. K.; Kanatzidis, M. G.; King, P.; Lancaster, K. M.; Lyman, S. V.; Pfromm, P.; Schneider, W. F.; Schrock, R. R. Beyond Fossil Fuel-Driven Nitrogen Transformations. *Science* **2018**, *360*, No. eaar6611.
- (5) Qing, G.; Ghazfar, R.; Jackowski, S. T.; Habibzadeh, F.; Ashtiani, M. M.; Chen, C.-P.; Smith, M. R.; Hamann, T. W. Recent Advances and Challenges of Electrocatalytic N<sub>2</sub> Reduction to Ammonia. *Chem. Rev.* **2020**, *120*, 5437–5516.
- (6) Rohr, B. A.; Singh, A. R.; Nørskov, J. K. A Theoretical Explanation of the Effect of Oxygen Poisoning on Industrial Haber-Bosch Catalysts. *J. Catal.* **2019**, *372*, 33–38.
- (7) Han, L.; Cai, S.; Gao, M.; Hasegawa, J.-y.; Wang, P.; Zhang, J.; Shi, L.; Zhang, D. Selective Catalytic Reduction of NO<sub>x</sub> with NH<sub>3</sub> by Using Novel Catalysts: State of the Art and Future Prospects. *Chem. Rev.* **2019**, *119*, 10916–10976.
- (8) Li, J.; Chang, H.; Ma, L.; Hao, J.; Yang, R. T. Low-Temperature Selective Catalytic Reduction of NO<sub>x</sub> with NH<sub>3</sub> over Metal Oxide and Zeolite Catalysts—A Review. *Catal. Today* **2011**, *175*, 147–156.
- (9) Wu, Q.; Wang, H.; Shen, S.; Huang, B.; Dai, Y.; Ma, Y. Efficient Nitric Oxide Reduction to Ammonia on a Metal-Free Electrocatalyst. *J. Mater. Chem. A* **2021**, *9*, 5434–5441.

- (10) Long, J.; Chen, S.; Zhang, Y.; Guo, C.; Fu, X.; Deng, D.; Xiao, J. Direct Electrochemical Ammonia Synthesis from Nitric Oxide. *Angew. Chem., Int. Ed.* **2020**, *59*, 9711–9718.
- (11) Katsounaros, I.; Figueiredo, M. C.; Chen, X.; Calle-Vallejo, F.; Koper, M. T. M. Structure- and Coverage-Sensitive Mechanism of NO Reduction on Platinum Electrodes. *ACS Catal.* **2017**, *7*, 4660–4667.
- (12) Choi, J.; Du, H.-L.; Nguyen, C. K.; Suryanto, B. H. R.; Simonov, A. N.; MacFarlane, D. R. Electroreduction of Nitrates, Nitrites, and Gaseous Nitrogen Oxides: A Potential Source of Ammonia in Dinitrogen Reduction Studies. *ACS Energy Lett.* **2020**, *5*, 2095–2097.
- (13) Farberow, C. A.; Dumesic, J. A.; Mavrikakis, M. Density Functional Theory Calculations and Analysis of Reaction Pathways for Reduction of Nitric Oxide by Hydrogen on Pt(111). *ACS Catal.* **2014**, *4*, 3307–3319.
- (14) Saeidi, N.; Esrafil, M. D.; Sardroodi, J. J. NO Electrochemical Reduction over Si-N<sub>4</sub> Embedded Graphene: A DFT Investigation. *Appl. Surf. Sci.* **2021**, *544*, 148869.
- (15) Wu, J.; Yu, Y.-X. A Theoretical Descriptor for Screening Efficient NO Reduction Electrocatalysts from Transition-Metal Atoms on N-doped BP Monolayer. *J. Colloid Interface Sci.* **2022**, *623*, 432–444.
- (16) Wu, Y.; Lv, J.; Xie, F.; An, R.; Zhang, J.; Huang, H.; Shen, Z.; Jiang, L.; Xu, M.; Yao, Q.; Cao, Y. Single and Double Transition Metal Atoms Doped Graphdiyne for Highly Efficient Electrocatalytic Reduction of Nitric Oxide to Ammonia. *J. Colloid Interface Sci.* **2024**, *656*, 155–167.
- (17) Chen, X.; Zhu, X.; Xia, Z.; Qian, S.; Zhou, Y.; Luo, Q.; Yang, J. 2D Conductive Metal–Organic Frameworks for NO Electrochemical Reduction: A First-Principles Study. *J. Mater. Chem. A* **2024**, *12*, 23612–23621.
- (18) Wu, Q.; Wei, W.; Lv, X.; Wang, Y.; Huang, B.; Dai, Y. Cu@g-C<sub>3</sub>N<sub>4</sub>: An Efficient Single-Atom Electrocatalyst for NO Electrochemical Reduction with Suppressed Hydrogen Evolution. *J. Phys. Chem. C* **2019**, *123*, 31043–31049.
- (19) Shahzad, F.; Iqbal, A.; Kim, H.; Koo, C. M. 2D Transition Metal Carbides (MXenes): Applications as an Electrically Conducting Material. *Adv. Mater.* **2020**, *32*, 2002159.
- (20) Fan, Y.; Li, L.; Zhang, Y.; Zhang, X.; Geng, D.; Hu, W. Recent Advances in Growth of Transition Metal Carbides and Nitrides (MXenes) Crystals. *Adv. Funct. Mater.* **2022**, *32*, 2111357.
- (21) Yu, Y.; Zhou, J.; Sun, Z. Novel 2D Transition-Metal Carbides: Ultrahigh Performance Electrocatalysts for Overall Water Splitting and Oxygen Reduction. *Adv. Funct. Mater.* **2020**, *30*, 2000570.
- (22) Chen, Z. W.; Lang, X. Y.; Jiang, Q. Discovery of Cobweb-like MoC<sub>6</sub> and Its Application for Nitrogen Fixation. *J. Mater. Chem. A* **2018**, *6*, 9623–9628.
- (23) Guo, L.; Zhou, J.; Liu, F.; Meng, X.; Ma, Y.; Hao, F.; Xiong, Y.; Fan, Z. Electronic Structure Design of Transition Metal-Based Catalysts for Electrochemical Carbon Dioxide Reduction. *ACS Nano* **2024**, *18*, 9823–9851.
- (24) Sher Shah, M. S. A.; Jang, G. Y.; Zhang, K.; Park, J. H. Transition Metal Carbide-based Nanostructures for Electrochemical Hydrogen and Oxygen Evolution Reactions. *EcoEnergy* **2023**, *1*, 344–374.
- (25) Bykov, M.; et al. High-Pressure Synthesis of Dirac Materials: Layered van Der Waals Bonded BeN<sub>4</sub> Polymorph. *Phys. Rev. Lett.* **2021**, *126*, 175501.
- (26) Zhang, S.; Feng, P.; Liu, D.; Wu, H.; Gao, M.; Xu, T.; Xie, Z. Y.; Yan, X.-W. Two-Dimensional Binary Transition Metal Nitride MN<sub>4</sub> (M = V, Cr, Mn, Fe, Co) with a Graphenelike Structure and Strong Magnetic Properties. *Phys. Rev. B* **2022**, *106*, 235402.
- (27) Liu, D.; Feng, P.; Zhang, S.; Gao, M.; Ma, F.; Yan, X.-W.; Xie, Z. Y. Prediction of Single-Atom-Thick Transition Metal Nitride CrN<sub>4</sub> with a Square-Planar Network and High-Temperature Ferromagnetism. *Phys. Rev. B* **2022**, *106*, 125421.
- (28) Sun, Y.; Duan, Y.; Li, X.; Xu, X.; Yao, X.; Liu, S.; Yin, H.; Wang, B.; Liu, Y.; Zhang, X. Intrinsic Magnetism with High Critical Temperatures and Piezoelectricity in 2D Transition Metal Tetaborides. *Int. J. Quantum Chem.* **2023**, *123*, No. e27117.
- (29) Qu, X.; Yang, J.; Wang, Y.; Lv, J.; Chen, Z.; Ma, Y. A Two-Dimensional TiB<sub>4</sub> Monolayer Exhibits Planar Octacoordinate Ti. *Nanoscale* **2017**, *9*, 17983–17990.
- (30) Savin, A.; Nesper, R.; Wengert, S.; Fässler, T. F. ELF: The Electron Localization Function. *Angew. Chem., Int. Ed. Engl.* **1997**, *36*, 1808–1832.
- (31) Liu, L.; Wang, C.; Zhang, L.; Liu, C.; Niu, C.; Zeng, Z.; Ma, D.; Jia, Y. Surface Van Hove Singularity Enabled Efficient Catalysis in Low-Dimensional Systems: CO Oxidation and Hydrogen Evolution Reactions. *J. Phys. Chem. Lett.* **2022**, *13*, 740–746.
- (32) Fan, D.; Chen, C.; Lu, S.; Li, X.; Jiang, M.; Hu, X. Highly Stable Two-Dimensional Iron Monocarbide with Planar Hypercoordinate Moiety and Superior Li-Ion Storage Performance. *ACS Appl. Mater. Interfaces* **2020**, *12*, 30297–30303.
- (33) Zhang, H.; Li, Y.; Hou, J.; Du, A.; Chen, Z. Dirac State in the FeB<sub>2</sub> Monolayer with Graphene-Like Boron Sheet. *Nano Lett.* **2016**, *16*, 6124–6129.
- (34) Zhang, H.; Li, Y.; Hou, J.; Tu, K.; Chen, Z. FeB<sub>6</sub> Monolayers: The Graphene-like Material with Hypercoordinate Transition Metal. *J. Am. Chem. Soc.* **2016**, *138*, 5644–5651.
- (35) Bafecky, A.; Stampfl, C.; Faraji, M.; Yagmurcukardes, M.; Fadlallah, M. M.; Jappor, H. R.; Ghergherehchi, M.; Feghhi, S. A. H. A Dirac-semimetal Two-Dimensional BeN<sub>4</sub>: Thickness-dependent Electronic and Optical Properties. *Appl. Phys. Lett.* **2021**, *118* (20), 203103.
- (36) Born, M.; Huang, K. In *Dynamical Theory Of Crystal Lattices*; Oxford University Press, 1996.
- (37) Wang, Z.-p.; Chen, Y.-j.; Fang, S.-y.; Zhang, X.-j.; Zhang, W.; Sun, F.-l.; Chen, W.-x.; Zhuang, G.-l. Magnetic Transition of 1D Ferromagnetic Catalysts during the NO Electroreduction. *J. Catal.* **2024**, *434*, 115524.
- (38) Yu, J.; Wang, Y.; Li, Y. A Two-Dimensional Covalent Organic Framework with Single-Atom Manganese for Electrochemical NO Reduction: A Computational Study. *Phys. Chem. Chem. Phys.* **2024**, *26*, 15120–15124.
- (39) Ko, B. H.; Hasa, B.; Shin, H.; Zhao, Y.; Jiao, F. Electrochemical Reduction of Gaseous Nitrogen Oxides on Transition Metals at Ambient Conditions. *J. Am. Chem. Soc.* **2022**, *144*, 1258–1266.